Computer Methods and Programs in Biomedicine 260 (2025) 108569

Contents lists available at ScienceDirect

Computer Methods and Programs in Biomedicine

journal homepage: www.sciencedirect.com/journal/computer-methods-and-programs-in-biomedicine

Planning transcatheter pulmonary valve implantation in the dysfunctional native RVOT: A semi-automated pipeline for dynamic analysis based on 4D-CT imaging

Francesco Sturla [a,b,1,*], Alessandro Caimi [c,1], Luca Giugno [d], Giulia Pasqualin [d], Karima Tissir [e], Francesco Secchi [f,g], Alberto Redaelli [b], Mario Carminati [d,2], Emiliano Votta [b,2]

[a] 3D and Computer Simulation Laboratory, IRCCS Policlinico San Donato, San Donato Milanese, Italy
[b] Department of Electronics, Information and Bioengineering, Politecnico di Milano, Milano, Italy
[c] Deparment of Civil Engineering and Architecture, Università degli Studi di Pavia, Pavia, Italy
[d] Department of Pediatric and Adult Congenital Cardiology, IRCCS Policlinico San Donato, San Donato Milanese, Italy
[e] Unit of Radiology, IRCCS Policlinico San Donato, San Donato Milanese, Italy
[f] Unit of Cardiovascular Imaging, IRCCS Multimedica, Sesto San Giovanni, Italy
[g] Department of Biomedical Sciences for Health, Università degli Studi di Milano, Milano, Italy

ARTICLE INFO

Keywords:
Native right ventricle outflow tract
Transcatheter pulmonary valve implantation
Computed tomography
Optical flow
Tetralogy of Fallot
Procedural planning

ABSTRACT

Background and objective: Dysfunction of the right ventricular outflow tract (RVOT) is a common long-term complication following surgical repair in patients with congenital heart disease. Transcatheter pulmonary valve implantation (TPVI) offers a viable alternative to surgical pulmonary valve replacement (SPVR) for treating pulmonary regurgitation but not all RVOT anatomies are suitable for TPVI. To identify a suitable landing zone (LZ) for TPVI, three-dimensional multiphase (4D) computed tomography (CT) is used to evaluate the size, shape, and dynamic behavior of the RVOT throughout the cardiac cycle. However, manually extracting measurements from multiplanar CT reformats is operator-dependent and time-consuming. Leveraging an optical-flow (OF) algorithm, we proposed a novel semi-automated pipeline for dynamic and comprehensive geometrical analysis of the RVOT anatomy.

Methods: Upon 4D-CT availability, at a pre-defined reference time-point, the patient-specific anatomy is semi-automatically segmented to generate the corresponding three-dimensional surface, which is navigated through a graphical user interface to define the mid-section of the potential LZ. Based on the axial length of the intended device, the proximal and distal LZ cross-sections are automatically identified. An OF-based algorithm is used to track the three LZ cross-sections frame by frame throughout the cardiac cycle, taking RVOT out-of-plane motion into account to update RVOT contours on each cross-section and to elaborate LZ geometrical changes. Finally, LZ time-dependent geometrical features are quantified and extracted.

Results: The pipeline was successfully applied to a retrospective cohort of patients, with OF-based tracking reporting excellent agreement ($r^2 = 0.99$) compared to manual processing, with a bias $< 1\%$ for both LZ area and perimeter, while also significantly improving time efficiency. CT-derived measurements extracted from LZ mid-section were the most influential covariates affecting the likelihood of TPVI feasibility. Among these, the minimum perimeter outperformed all other geometric LZ parameters in classifying patients as suitable for either

Abbreviations: 3D, three-dimensional; A, area; Ao, aorta; AUC, area under the curve; BE, balloon-expandable; CI, confidence interval; CHD, congenital heart disease; CT, computed tomography; D_A, diameter from area; D_H, hydraulic diameter; D_P, diameter from perimeter; e, eccentricity; LA, left atrium; LV, left ventricle; LZ, landing zone; ma, minor semi-axes; MA, major semi-axes; MRI, magnetic resonance imaging; OF, optical flow; OR, odd ratio; PDF, probability density function; P, perimeter; PA, pulmonary artery; PR, pulmonary regurgitation; PS, pulmonary stenosis; PV, pulmonary valve; RA, right atrium; RF, regurgitant fraction; ROI, region of interest; RV, right ventricle; RVOT, right ventricular outflow tract; SD, standard deviation; SPVR, surgical pulmonary valve replacement; THV, transcatheter heart valve; ToF, Tetralogy of Fallot; TPVI, transcatheter pulmonary valve implantation; TTE, transthoracic echocardiography.

* Corresponding author.
E-mail address: francesco.sturla@grupposandonato.it (F. Sturla).
[1] Francesco Sturla and Alessandro Caimi equally contributed to first authorship.
[2] Mario Carminati and Emiliano Votta are equally contributing principal investigators.

https://doi.org/10.1016/j.cmpb.2024.108569
Received 23 October 2024; Received in revised form 5 December 2024; Accepted 16 December 2024
Available online 17 December 2024

TPVI or SPVR and achieved the highest area under the curve of 0.99, with accuracy and precision of 0.93 and 0.92, respectively.
Conclusions: Dynamic OF-based quantification of key RVOT geometric parameters can enhance and expedite the selection process for TPVI candidates and guide optimal valve sizing during TPVI planning.

1. Introduction

In around 20% of cases, congenital heart diseases (CHD) involve the right ventricular outflow tract (RVOT) and the pulmonary valve (PV) [1]. In particular, Tetralogy of Fallot (ToF) is the most common form of cyanotic CHD, and accounts for 10% of all CHD defects [2]. Surgical correction of cyanotic CHD is usually performed in infancy or early childhood and based on transannular patchplasty or valve-sparing repair [3]. In most patients it results in progressive RV dysfunction due to longstanding free pulmonary regurgitation and residual obstruction, which may lead to symptomatic heart failure, ventricular arrhythmias and risk of sudden death [4,5]. As a consequence, these patients may require PV replacement, which can be performed through surgical pulmonary valve replacement (SPVR) or through transcatheter pulmonary valve implantation (TPVI), with the latter representing a low-risk alternative to surgery in selected patients with a suitable RVOT anatomy [6–8]. To this aim, a wide range of transcatheter heart valves (THVs) is currently available; their suitability and effectiveness depend on the anatomy and the dynamics of the native RVOT. The balloon-expandable Melody® (Medtronic, Minneapolis, MN, USA) THV, which was the first THV used to perform TPVI [9], is commonly used in patients with a stenotic RVOT conduit [10] and its off-label use to treat the native RVOT has been reported in patients with a small RVOT caliber [11]. The Sapien® (Edwards Lifesciences, Irvine, CA, USA) THV, whose implants yielded most of the current evidence for TPVI with balloon-expandable devices, allows for treating larger RVOTs, as it is currently available in external diameters up to 29 mm [12,13]. Specifically, both Sapien XT and the Sapien 3 versions are approved for use in patients with a dysfunctional, previously repaired or replaced non-compliant RVOT [14]. Furthermore, preliminary data have been recently reported about the initial experience of the Myval (Meril Life Sciences, Gujarat, India) THV use in the native RVOT [15]. However, the design of these balloon-expandable THVs, along with the available sizes, makes their application more challenging when the RVOT anatomy is either too large or too distensible, which may lead to device migration or embolization (i.e., the unexpected dislodgement of the device into the RV) [11,16]. Accordingly, to extend TPVI to patients with larger native RVOTs, a new TPVI paradigm based on self-expandable THVs (e.g., Venus P-valve, Harmony and Pulsta) has recently emerged and is currently under clinical evaluation [10].

Though self-expandable THVs are intended to improve implant stability within the native RVOT, there are several anatomical scenarios that can be effectively tackled only through balloon expandable THVs: e.g., hypoplasic pulmonary arteries, stented or complex pulmonary branches, short pulmonary trunk and TPVI into a single pulmonary artery branch [17,18].

There is actually a wide variety of RVOT features that should be assessed pre-operatively when selecting candidates [19–21]: shape (e.g., cylindrical, fusiform, pyramidal), size (i.e., cross-sectional dimensions and ellipticity, and axial extent), and dynamic behavior (i.e., changes in axial extent and in cross-sectional dimensions and shape during the cardiac cycle). Furthermore, as a consequence of the previous surgery at pediatric age and progression of RVOT dysfunction over time, the anatomy of the native and patched RVOT is complex and such assessment may be particularly challenging [22]. Indeed, the RVOT anatomy is typically enlarged and heterogenous in shape and size, e.g., due to localized aneurysmal dilatation, as well as in compliance, e.g., due to the presence of a pericardial patch on one side of the native RVOT [11,23].

On this basis, it is reasonable to state that the most exhaustive and reliable characterization of RVOT anatomy should be fully 3D and dynamic, i.e., over the cardiac cycle, to identify a suitable landing zone (LZ) for TPVI. The LZ refers to the specific region within the RVOT where the THV is intended to be implanted, ensuring fixation, stability, and function of the THV [24]. This would be feasible by leveraging three-dimensional (3D) contrast-enhanced ECG-gated computed tomography (CT) imaging, frequently referred to as 4D-CT. However, to date, the potential of this image modality is only partially exploited since the analysis is limited to only a few phases of the cardiac cycle, typically end-systole and end-diastole [21]. This is mainly due to the fact that, as reported in recently published studies and guidelines [19,22,25], the landing zone (LZ) is measured by manual tracings on specific user-defined cut-planes. Accordingly, measurements not only are operator-dependent but also time-consuming.

To tackle these limitations, herein we propose a novel semi-automated pipeline to predict the feasibility of TPVI on a patient-specific basis. The pipeline was designed to exhaustively and efficiently quantify the anatomy of the dysfunctional RVOT and of the potential LZ over the cardiac cycle based on 4D-CT imaging.

2. Methods

2.1. Pipeline

The developed pipeline involves four main steps (Fig. 1, Algorithm 1):

i. RVOT/PA segmentation and 3D surface reconstruction at the reference time-point (Section 2.1.1): from 4D-CT imaging, 3D triangulated surfaces of PA and RVOT wall are generated within a global cartesian coordinate system through semi-automatically segmentation of the RVOT and the PA. Additionally, a set of consecutive points representing the RVOT/PA centerline is generated and exported.
ii. Navigation of RVOT/PA anatomy and LZ definition (Section 2.1.2): through an ad hoc graphical user interface, the RVOT/PA 3D geometry is navigated to identify the mid-section of the potential LZ, whose proximal and distal cross-sections are then automatically determined. The intersection of each cross-section with the RVOT/PA surface is extracted using Fourier contour approximations, which allow contour smoothing, regularization, and uniform resampling. Also, two mutually orthogonal longitudinal planes are automatically generated to guide the subsequent dynamic tracking of LZ cross-sections.
iii. Optical flow tracking of LZ cross-sections (Section 2.1.3): an algorithm leveraging optical flow (OF) and linear voxel interpolation of the CT image volume is employed to automatically track the three LZ cross-sections during the cardiac cycle. This approach accounts for out-of-plane motion, updates RVOT contours on each cross-section and quantifies the dynamic changes in LZ geometry.
iv. Quantification of LZ time-dependent geometrical features (Section 2.1.4): the time-course of LZ geometrical features – such as area, perimeter and the corresponding equivalent diameters - is automatically computed for each cross-section. Additionally, the minimum, mean, and maximum values of each parameter are extracted over the cardiac cycle.

2.1.1. RVOT/PA segmentation and 3D surface reconstruction at the reference time-point

The blood pool within both the native RVOT and the aortic root were segmented at the reference frame (phase 0) of the 4D-CT acquisition using the commercial Mimics Innovation Suite (Mimics Medical 25.0 and 3-matic Medical 17.0, Materialise, Leuven, Belgium). Anatomical semi-automatic segmentation was performed by a certified operator using the CT Heart tool (Mode = "Manual", Region of interest = "Full Heart"). After initial delineation of the box containing the overall anatomical region of interest (ROI), separate threshold value ranges were defined for the left heart (LA, left atrium; LV, left ventricle; Ao, aorta) and right heart (RA, right atrium; RV, right ventricle; PA, pulmonary artery) masks by dragging the boundaries of the corresponding thresholding histogram. Seed points, at least one for each left and right sub-regions, were manually positioned to automatically identify and separate the masks of the segmented anatomical sub-regions. Subsequently, the "Calculate Part" command (Quality = "Optimal") was used to automatically create a 3D object for PA and Ao masks (Fig. 1a). Trimming operation (Trim) was performed in 3-matic to locally trim excess of material for each 3D object. The "Wrap" operation was then used to filter small inclusions and close small holes ("Gap closing distance" = 1.0 mm; "Small detail" = 1.0 mm)

Subsequently, Ao and RVOT/PA blood pool isosurfaces (Ω^0_{Ao} and Ω^0_{PA}, respectively) were generated as separate 3D triangulated surfaces and the "Fit Centerline Curve" tool [26] was used to automatically calculate the RVOT/PA centerline ($\boldsymbol{X}^0_{PA}$) ("Segment length" = 0.5 mm; "Detail" = 0.5 mm) as a set of consecutive points.

The coordinates of the points in $\boldsymbol{X}^0_{PA}$ and of the vertices in Ω^0_{Ao} and Ω^0_{PA} were automatically transformed from the image reference frame (*rcs*, with *r, c* and *s* representing the row, column and slice indexes of the image volume) into the global cartesian coordinate system (*xyz*) based on the metadata available in the DICOM files. Briefly, the single image voxel $\boldsymbol{I}(I_r,I_c,I_s)$ was mapped to the cartesian position $\boldsymbol{P}(P_x,P_y,P_z)$ through the following transformation:

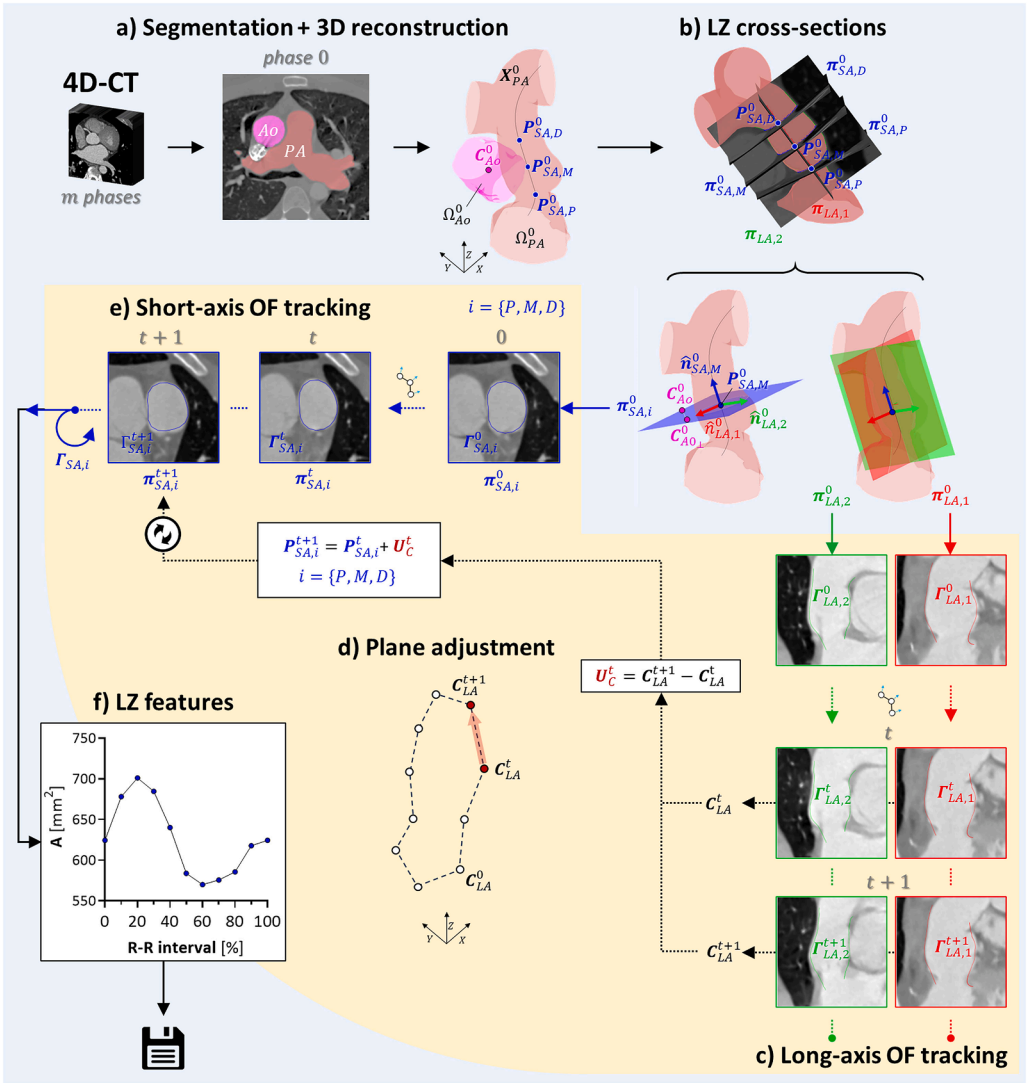

Fig. 1. Developed pipeline: 4D-CT imaging and user-defined input data (a) are required and, after CT image volume mapping to the global cartesian reference system (b), used to initialize the landing zone (LZ) cross-sections. Frame by-frame optical flow (OF)-based tracking of the RVOT/PA contours is performed on long-axis (LA) planes (c). At each frame, the incremental displacement ($\boldsymbol{U}_C^{t+1}$) of the centroid ($\boldsymbol{C}_{LA}^t$) of the LA contours ($\boldsymbol{\Gamma}_{LA,j}^t$, $j = 1,2$) is computed and used to create adjusted short-axis (SA) planes $\boldsymbol{\pi}_{SA,i}^{t+1}$, $i = P, M, D$ (d). OF-based optical tracking of the SA contours $\boldsymbol{\Gamma}_{SA,i}^t$, $i = P, M, D$ is performed from $\boldsymbol{\pi}_{SA,i}^t$ to $\boldsymbol{\pi}_{SA,i}^{t+1}$ (e). Finally, geometrical analysis is accomplished on each cross-section (f).

Algorithm 1
Assessment of LZ geometry changes from 4D CT.

select initial segmented phase ($t = 0$) from 4D-CT imaging (m cardiac phases available)
input data: RVOT/PA 3D surface (Ω^0_{PA}) and centerline ($\boldsymbol{X}^0_{PA}$); aortic root 3D surface (Ω^0_{Ao})
user input for intended LZ (length = l): central reference point $\boldsymbol{P}^0_{SA,M} \in \boldsymbol{X}^0_{PA}$
mid LZ plane $\boldsymbol{\pi}^0_{SA,M}$: origin $\boldsymbol{P}^0_{SA,M}$ and normal unit vector $\widehat{\boldsymbol{n}}^0_{SA,M}$ tangent to $\boldsymbol{X}^0_{PA}$
proximal LZ plane $\boldsymbol{\pi}^0_{SA,P}$: origin $\boldsymbol{P}^0_{SA,P} \in X^0_{PA}$,

$\overrightarrow{P^0_{SA,P}P^0_{SA,M}} = \frac{l}{2}\,\widehat{\boldsymbol{n}}^0_{SA,P}$ tangent to $\boldsymbol{X}^0_{PA}$ in $\boldsymbol{P}^0_{SA,P}$

distal LZ plane $\boldsymbol{\pi}^0_{SA,D}$: origin $P^0_{SA,D} \in X^0_{PA}$,

$\overrightarrow{\boldsymbol{P}^0_{SA,M}\boldsymbol{P}^0_{SA,D}} = \frac{l}{2}\,\widehat{\boldsymbol{n}}^0_{SA,D}$ tangent to $\boldsymbol{X}^0_{PA}$ in $\boldsymbol{P}^0_{SA,D}$

Fourier approximated contours $\boldsymbol{\Gamma}^0_{SA,i}$ intersecting Ω^0_{PA} on $\boldsymbol{\pi}^0_{SA,i}$, $i = \{M, P, D\}$
compute LZ geometrical features at phase 0 on $\boldsymbol{\pi}^0_{SA,i}$
$\mathbf{C}^0_{Ao}$ centroid projection on $\boldsymbol{\pi}^0_{SA,M} \rightarrow \mathbf{C}^0_{Ao_\perp}$
longitudinal plane $\boldsymbol{\pi}^0_{LA,1}$: origin $\boldsymbol{P}^0_{SA,M}$, normal $\widehat{\boldsymbol{n}}^0_{LA,1} = \overrightarrow{\boldsymbol{P}^0_{SA,M}\mathbf{C}^0_{Ao}{}^{\perp}}$
longitudinal plane $\boldsymbol{\pi}^0_{LA,2}$: origin $\boldsymbol{P}^0_{SA,M}$, normal $\widehat{\boldsymbol{n}}^0_{LA,2} = \widehat{\boldsymbol{n}}^0_{SA,M} \times \widehat{\boldsymbol{n}}^0_{LA,1}$
Fourier approximated contours $\boldsymbol{\Gamma}^0_{LA,j}$, $j = \{1, 2\}$, intersecting Ω^0_{PA} on $\boldsymbol{\pi}^0_{LA,j}$
$\cup^2_{j=1}\boldsymbol{\Gamma}^0_{LA,j} \rightarrow$ compute longitudinal centroid $\boldsymbol{C}^0_{LA}$
linear voxel CT volume interpolation on $\boldsymbol{\pi}^0_{SA,i}$, $i = \{M, P, D\}$ and $\boldsymbol{\pi}^0_{LA,j}$, $j = \{1, 2\}$
for $t = 0$ to $(m - 1)$
    OF-based tracking: $\boldsymbol{\Gamma}^t_{LA,j} \rightarrow \boldsymbol{\Gamma}^{t+1}_{LA,j}$, $j = \{1, 2\}$
    $\cup^2_{j=1}\boldsymbol{\Gamma}^{t+1}_{LA,j} \rightarrow$ compute $\boldsymbol{C}^{t+1}_{LA}$
    calculate displacement $\boldsymbol{U}^t_C = \boldsymbol{C}^{t+1}_{LA} - \boldsymbol{C}^t_{LA}$
    switch $i = \{M, P, D\}$
        $\dot{\boldsymbol{P}}^{t+1}_{SA,i} = \boldsymbol{P}^t_{SA,i} + \boldsymbol{U}^{t+1}_C$
        $\boldsymbol{P}^{t+1}_{SA,i} \in \boldsymbol{X}^0_{PA}$: $\overline{\boldsymbol{P}^{t+1}_{SA,i}\dot{\boldsymbol{P}}^{t+1}_{SA,i}} = \min$
        adjust $\boldsymbol{\pi}^{t+1}_{SA,i}$, $\widehat{\boldsymbol{n}}^{t+1}_{SA,i}$ tangent to $\boldsymbol{X}^0_{PA}$
        linear voxel CT volume interpolation on $\boldsymbol{\pi}^{t+1}_{SA,i}$
        OF-based tracking: $\boldsymbol{\Gamma}^t_{SA,i} \rightarrow \boldsymbol{\Gamma}^{t+1}_{SA,i}$
        compute LZ geometrical features at phase $(t + 1)$ on $\boldsymbol{\Gamma}^{t+1}_{SA,i}$
    end switch
end for
switch $i = \{M, P, D\}$
    extract $x_{i,min}$, $x_{i,mean}$, $x_{i,MAX}$ $\forall$ time-dependent LZ feature $x(t)$
    compute relative percentage change $RxC_i \forall\ x(t)$
end switch

$$\begin{bmatrix} P_x \\ P_y \\ P_z \\ 1 \end{bmatrix} = \begin{bmatrix} r_x v_r & c_x v_c & \dfrac{x_n - x_1}{n-1} & x_1 \\ r_y v_r & c_y v_c & \dfrac{y_n - y_1}{n-1} & y_1 \\ r_z v_r & c_z v_c & \dfrac{z_n - z_1}{n-1} & z_1 \\ 0 & 0 & 0 & 1 \end{bmatrix} \begin{bmatrix} I_r \\ I_c \\ I_s \\ 1 \end{bmatrix}$$

where the two triplets $[r_x, r_y, r_z, c_x, c_y, c_z]$ are provided by the DICOM tag of *Image Orientation Patient* and encode the direction cosines of the row and column of an image slice, respectively, expressed in the cartesian xyz reference system; the vector $[x_1, y_1, z_1]$ represents the *Image Position Patient* of the first slice (in mm), namely the cartesian coordinates of the upper-left corner voxel, and $[x_n, y_n, z_n]$ the *Image Position Patient* of the last slice in the image volume; v_r and v_c determine the row and column spatial resolution (in mm) and are stored in the *Pixel Spacing* DICOM tag; n is the number of slices in the image volume.

The cartesian coordinates of the points in $\boldsymbol{X}^0_{PA}$ were exported to a text (.txt) file. Vertex coordinates and connectivity of Ω^0_{Ao} and Ω^0_{PA} were exported as stereolithography (.stl) files; Ω^0_{Ao} and $\Omega^0_{PA}\Omega_{PA}$ were then remeshed in Meshmixer (Autodesk, San Rafael, CA, USA) with a characteristic triangle size (l) of 0.6 mm.

2.1.2. Navigation of RVOT and PA and LZ definition

The content of the .txt and .stl files was automatically rendered through a graphical user interface allowing to navigate the 3D anatomy of the RVOT and PA having the centroid of the aortic root ($\boldsymbol{C}^0_{Ao}$) as landmark, and to easily define the mid-section of the potential LZ by selecting a position ($\boldsymbol{P}^0_{SA,M}$) on $\boldsymbol{X}^0_{PA}$ (Fig. 1b). This selection triggered the following automatic generation of:

- the mid short-axis, i.e., cross-sectional, plane $\boldsymbol{\pi}^0_{SA,M}$ running through $\boldsymbol{P}^0_{SA,M}$ and normal to $\widehat{\boldsymbol{n}}^0_{SA,M}$, which approximated the unit vector tangent to $\boldsymbol{X}^0_{PA}$ in $\boldsymbol{P}^0_{SA,M}$ as the normalized vector connecting $\boldsymbol{P}^0_{SA,M}$ with the subsequent distal point of $\boldsymbol{X}_{PA}$.
- the proximal ($\boldsymbol{\pi}_{SA,P}$) and the distal ($\boldsymbol{\pi}_{SA,D}$) cross-sectional planes delimiting the LZ. Given an axial extent (L_{LZ}) of the device to be implanted, their origins ($\boldsymbol{P}^0_{SA,P}$ and $\boldsymbol{P}^0_{SA,D}$) were identified at a curvilinear distance $L_{LZ}/2$ along $\boldsymbol{X}^0_{PA}$ upstream from and downstream of the origin of central cross-section $\boldsymbol{\pi}_{SA,M}$, respectively. Their respective outward normal vectors ($\widehat{\boldsymbol{n}}^0_{SA,P}$ and $\widehat{\boldsymbol{n}}^0_{SA,D}$, respectively) were equal to the respective unit local tangent vector to $\boldsymbol{X}^0_{PA}$.
- the intersections ($\boldsymbol{\Gamma}^0_{SA,i}, i = P, M, D$) between Ω^0_{PA} and each cross-sectional plane $\boldsymbol{\pi}^0_{SA,i}$, $i = P, M, D$. For each cross-sectional plane $\boldsymbol{\pi}^0_{SA,i}$, the nodes of Ω^0_{PA} distant no more than $l/2$ (i.e., 0.3 mm) from $\boldsymbol{\pi}^0_{SA,i}$ were identified, and their projections on $\boldsymbol{\pi}^0_{SA,i}$ were computed and fitted to obtain a regular and dense profile of the relevant cross section. Namely, in a cylindrical local reference $\rho\vartheta z'$ frame with origin in $\boldsymbol{P}^0_{SA,i}$ and local z'-axis equal to $\widehat{\boldsymbol{n}}^0_{SA,i}$ the radial position (ρ) of each projection was approximated through a 4th order Fourier function of the angular position (ϑ) in the form:

$$\rho(\vartheta) = a_0 + \sum_{k=1}^{4}\left[a_k \cdot \sin(k\vartheta) + b_k \cdot \cos(k\vartheta)\right]$$

where a_0, a_k and b_k are the coefficients of the Fourier function; the final $\boldsymbol{\Gamma}^0_{SA,i}$ profile was sampled uniformly.

- two mutually orthogonal longitudinal planes ($\boldsymbol{\pi}^0_{LA,1}$ and $\boldsymbol{\pi}^0_{LA,2}$) perpendicular to $\boldsymbol{\pi}^0_{SA,M}$ and passing through $\boldsymbol{P}^0_{SA,M}$. $\boldsymbol{\pi}^0_{LA,1}$ was computed as the plane passing through the projection ($\boldsymbol{C}^0_{Ao,\perp}$) of $\boldsymbol{C}^0_{Ao}$ on $\boldsymbol{\pi}^0_{SA,M}$ and normal to the unitary vector $\widehat{\boldsymbol{n}}^0_{LA,1}$ directed from $\boldsymbol{P}^0_{SA,M}$ to $\boldsymbol{C}_{Ao,\perp}$. For $\boldsymbol{\pi}^0_{LA,2}$, the unitary normal vector $\widehat{\boldsymbol{n}}^0_{LA,2}$ was defined as the cross product between $\widehat{\boldsymbol{n}}^0_{SA,M}$ and $\widehat{\boldsymbol{n}}^0_{LA,1}$. For each longitudinal plane $\boldsymbol{\pi}^0_{LA,j}$, $j = 1, 2$, the intersection $\boldsymbol{\Gamma}^0_{LA,j}$ with Ω^0_{PA} was computed and consisted of two distinct contours on opposite sides of the RVOT/PA lumen (Fig. 1c). The nodes of Ω^0_{PA} satisfying two conditions were selected: i) distance no greater than l/2 from $\boldsymbol{\pi}^0_{LA,j}$; ii) position within two short-axis planes passing through points located 5 mm proximal to $\boldsymbol{\pi}^0_{SA,P}$ and 5 mm distal to $\boldsymbol{\pi}^0_{SA,D}$. The selected nodes were projected onto $\boldsymbol{\pi}^0_{LA,j}$, clustered into two distinct clouds, and reordered based on the longitudinal plane orientation, yielding the points of the two contours. Each contour was smoothed using a Savitzky-Golay quadratic polynomial filter [27].

2.1.3. Optical flow tracking of LZ cross-sections

The changes in LZ geometry at the $\boldsymbol{\Gamma}^0_{SA,M}$, $\boldsymbol{\Gamma}^0_{SA,P}$ and $\boldsymbol{\Gamma}^0_{SA,D}$ cross-sections during the cardiac cycle were automatically quantified through a dedicated pipeline leveraging an OF algorithm [28] (Fig. 1c-e).

Within the cartesian reference system, at every phase t, with t being initially equal to 0, linear voxel interpolation of the CT image volume was performed on $\boldsymbol{\pi}^t_{LA,1}$ and $\boldsymbol{\pi}^t_{LA,2}$, and interpolated values were resampled using a pre-defined 70 × 70 mm squared grid with a pixel spacing of 0.175 mm. At phase 0, all the image pixels on $\boldsymbol{\Gamma}^0_{LA,1}$ and $\boldsymbol{\Gamma}^0_{LA,2}$ were recognized and tracked frame-by-frame on the corresponding cutting plane, yielding $\boldsymbol{\Gamma}^t_{LA,1}$ and $\boldsymbol{\Gamma}^t_{LA,2}$, with $t = 0, \ldots, m-1$(m cardiac phases available).

The centroid ($\boldsymbol{C}^t_{LA}$) of the four contours obtained on the two planes is computed. Hence, given two consecutive phases t and $t+1$, the intercurring displacement of the centroid ($\boldsymbol{U}^{t+1}_C = \boldsymbol{C}^{t+1}_{LA} - \boldsymbol{C}^t_{LA}$) is computed. $\boldsymbol{U}^{t+1}_C$ was used to adjust the OF-based tracking in the SA planes: given a SA plane $\boldsymbol{\pi}^t_{SA,i}$, $i = P, M, D$, at phase t passing through the point $\boldsymbol{P}^t_{SA,i}$ of the centerline $\boldsymbol{X}^0_{PA}$ and orthogonal to the unitary vector $\hat{\boldsymbol{n}}^t_{SA,i}$, an adjusted plane $\boldsymbol{\pi}^{t+1}_{SA,i}$ is defined by an origin $\boldsymbol{P}^{t+1}_{SA,i}$, i.e., the point of the centerline $\boldsymbol{X}^0_{PA}$ closest to the position $\tilde{\boldsymbol{P}}^{t+1}_{SA,i} = \boldsymbol{P}^t_{SA,i} + \mathbf{U}^{t+1}_C$, and the unitary vector $\hat{\boldsymbol{n}}^{t+1}_{SA,i}$ that identifies the tangent to $\boldsymbol{X}^0_{PA}$ in $\boldsymbol{P}^{t+1}_{SA,i}$ (Fig. 1d).

Upon linear voxel interpolation of the CT image volume on $\boldsymbol{\pi}^t_{SA,i}$ and $\boldsymbol{\pi}^{t+1}_{SA,i}$ and resampling through the previously mentioned squared grid, the SA profile $\boldsymbol{\Gamma}^t_{SA,i}$ is tracked from $\boldsymbol{\pi}^t_{SA,i}$ to $\boldsymbol{\pi}^{t+1}_{SA,i}$ by the same OF algorithm (Fig. 1e).

2.1.4. Quantification of LZ time-dependent geometrical features

Time-dependent geometrical area (A) and perimeter (P) were automatically computed for each cross-section $\boldsymbol{\Gamma}^t_{SA,i}$ over the cardiac cycle; standardized diameters were calculated from the perimeter (D_P), considering each section equivalent to a circle with perimeter P, and from the area (D_A), considering each section equivalent to a circle with area A. Also, the hydraulic diameter (D_H) was defined as [29]:

$$D_H = \frac{(4 \cdot A)}{P}$$

Furthermore, through a direct least square fitting algorithm for scattered data [30], the points of each cross-section were fitted with an ellipse to compute its major (MA) and minor (ma) semi-axes as well as its eccentricity (e):

$$e = \sqrt{1 - MA^2/ma^2}$$

where $e = 0$ for a circle and $0 < e < 1$ for an elliptical shape.

For each analyzed time-dependent parameter $x(t)$, the minimum (x_{min}), mean (x_{mean}) and maximum (x_{MAX}) values were extracted over the cardiac cycle for each plane. Also, the corresponding relative percentage change was calculated on each short-axis plane as:

$$RxC = 100 \cdot \frac{x_{MAX} - x_{\min}}{x_{\min}}$$

2.2. Pipeline application to a retrospectively selected population of TPVI candidates

2.2.1. Study cohort

To test our pipeline, 45 patients were retrospectively selected out of 77 consecutive patients diagnosed with post-surgical RVOT dysfunction and referred to TPVI or SPVR, if TPVI was deemed inadequate, in the tertiary-care Department of Pediatric and Adult Congenital Cardiology of IRCCS Policlinico San Donato (San Donato Milanese, Milan, Italy), between January 2016 and December 2020. The local Ethics Committee approved the study (research protocol code "4D_Native_RVOT", No. 56/INT/2022, accepted on June 24th, 2022) and informed consent was waived due to the retrospective nature of the study and the analysis of anonymized data. The study was conducted in compliance with the Good Clinical Practice and Declaration of Helsinki principles.

The 45 patients were included in the study according to the following inclusion criteria: i) diagnosis of dysfunctional native RVOT requiring repair for severe pulmonary valve regurgitation through TPVI with balloon-expandable THV or SPVR; ii) age between 10 and 70 years old; iii) balloon-expandable TPVI with THV diameter size of 29 mm (Sapien or Myval THVs), or SPVR if deemed preferable due to native RVOT dimension; iv) availability of preoperative ECG-gated 4D-CT examination with full multiphase coverage, i.e., from 0% to 100% of the cardiac cycle with a 10% increment. The following exclusion criteria were adopted: (i) ECG-gated 4D-CT not available; (ii) ECG-gated 4D-CT imaging only partially covering the cardiac cycle (e.g., sequential 4D-CT with only partial coverage of systole or diastole); (iii) low quality of 4D-CT imaging; (iv) previous TPVI (i.e., patients requiring valve-in-valve TPVI); (v) SPVR required for specific reasons in addition to severe pulmonary valve regurgitation only; (vi) TPVI with balloon-expandable THV with diameter size < 29 mm; (vi) TPVI rejected after diagnostic catheterization with no subsequent SPVR. The final indication for TPVI was confirmed by the heart team through diagnostic catheterization, consisting in balloon-testing, prior to TPVI. Baseline patient characteristics as well as procedural data in patients referred to TPVI were retrieved from clinical records; the clinical outcomes available at discharge and last follow up are provided in the supplementary material (Table S1). Out of the 45 selected TPVI candidates, 22 patients underwent TPVI with a balloon-expandable device while the remaining 23 were referred to SPVR (Table 1). Among TPVI recipients, 17 patients received the Sapien 29, and 6 patients were implanted with the Myval 29, both devices having a nominal valve diameter of 29 mm.

2.2.2. 4D-CT acquisition

Each patient underwent CTA examination in supine position in a 64-slice dual-source SOMATOM Definition AS multidetector system (Siemens, Erlangen, Germany) with retrospective ECG-gating.

Multi-phase images, encompassing the heart, proximal aorta and the pulmonary arteries, were recorded at each 10% increment of the cardiac cycle, i.e., from 0% to 100% with respect to R-R interval. The acquisition field of view was set to 500 mm and image reconstruction was performed by means of a convolution B26f kernel on a 512 × 512 matrix; nominal slice thickness was ≤ 1.5 mm for all datasets. Test bolus with a small amount of contrast (5 mL) was initially injected to evaluate the time of the contrast reaching the pulmonary artery and calculate the delay time between contrast injection and the start of the scan [31]. Subsequently, contrast medium (Iomeron 400 mgI/ml, Bracco, Italia) was injected in a single bolus at a rate between 4 and 5 ml/s with an overall volume of 80 ml of contrast solution depending on the patient. CT scan parameters are summarized in Table 2. According to [23], the type of LZ morphology was also registered (Table 1).

Table 1
Demographic and morphometric characteristics of enrolled patients.

Variable		SPVR (n = 22)	TPVI (n = 23)	P value[§]
Age[1], y		29 ± 13	33 ± 18	0.30
Female, n (%)		10 (45.5)	11 (47.8)	0.99
Height, cm		164 ± 16	161 ± 12	0.47
Weight, Kg		58 ± 17	56 ± 14	0.70
BSA[2], m^2		1.67 [1.30, 1.89]	1.56 [1.30, 1.79]	0.39
RVOT type[■]	I	8 (36.4)	8 (34.8)	–
	II	7 (31.8)	0 (0.0)	
	III	4 (18.2)	7 (30.4)	
	IV	0 (0.0)	0 (0.0)	
	V	3 (13.6)	8 (34.8)	

Data presented as mean ± SD, median [IQR] or n (%).
[1] Age registered at pre-procedural CT examination.
[2] Body surface area (BSA) computed according to Du Bois.
[§] Unpaired t-test or Mann-Whitney test according to data normality.
[■] Classification of RVOT type according to [23].

Table 2
Key scan parameters adopted for 4D CT acquisitions included in the retrospective analysis.

Parameter	Range*
Tube potential (kV)	80 ÷ 120
Radiation dose (mAs)	42 ÷ 215
Tube current (mA)	128 ÷ 650
Reconstruction FOV (mm)	142 ÷ 254
Pixel spacing (mm)	0.28 ÷ 0.50
Slice thickness (mm)	0.6 ÷ 1.5
Pitch factor (-)	0.20 ÷ 0.46

* Values expressed as minimum ÷ maximum values.
FOV, field of view.

2.2.3. Pipeline setting

The 3D pipeline was used for dynamic assessment of LZ geometry in the 45 selected TPVI candidates. Phase 0 was the 30% frame of the cardiac cycle corresponding to 30% of the R-R interval within the 4D-CT image sequence. Consistently with the use of a balloon-expandable device, L_{LZ} was set to 20 mm.

2.2.4. Statistics and data presentation

Statistical analyses were performed using IBM SPSS Statistics software (version 22.0, IBM Corporation, Armonk, New York). Continuous variables were expressed as mean ± standard deviation (SD) or median [25th, 75th percentile] according to the Shapiro-Wilk normality test; comparisons were accomplished through unpaired Student's *t*-test for normal distribution and Mann-Whitney U test for not normally distributed data.

After normality test, geometrical LZ parameters were compared using two-way analysis of variance considering group (TPVI vs. SPVR) and plane position (proximal, mid or distal) as independent factors; a P value < 0.05 was considered statistically significant. Differences between manual and OF-based calculation of geometrical features (i.e., A and P) were assessed through Bland-Altman plots on a subset of 15 randomly selected patients, comparing the two approaches on three different planes throughout the cardiac cycle. Correlations were assessed by means of linear regression.

Standard logistic regression analysis was carried out to ascertain the effect of LZ geometrical descriptors on the likelihood of TPVI feasibility according to the clinical decision. For each variable, measures extracted from the proximal, mid and distal LZ tracked planes were entered into the model; precision of odd ratios (ORs) was determined through the 95% confidence interval (CI) and the Nagelkerke R^2 statistics was employed to assess the explained variation in the dependent variables based on the model. Observed and predicted classifications were examined to assess the effectiveness of each model prediction against the actual clinical classification, also assessing the area under the curve (AUC) of the corresponding receiver-operating characteristic (ROC) curve.

Finally, a probability density function (PDF) was estimated for the most relevant LZ parameters through a bimodal model of the form:

$$PDF(x) = \frac{n_{TPVI}}{n_{TPVI}+n_{SPVR}} \cdot N(\mu_{TPVI}, \sigma_{TPVI}, x) + \frac{n_{TPVI}}{n_{TPVI}+n_{SPVR}} \cdot N(\mu_{SPVR}, \sigma_{SPVR}, x)$$

where x is the considered LZ parameter, $N(\mu_i,\sigma_i,x)$ is the PDF of x reported as a normal distribution centered at μ_i and with standard deviation σ_i (i equal to TPVI and SPVR, respectively), n_{TPVI} and n_{SPVR} denote the number of patients in each group. To assess the level of separation between the two groups in the bimodal distribution, the Ashman's D was computed [32]:

$$D = 2^{\frac{1}{2}} \frac{|\mu_1 - \mu_2|}{\sqrt{\sigma_1^2 + \sigma_2^2}}$$

according to which, for a mixture of two normal distributions, $D \geq 2$ is required to recognize a clean separation between two groups.

3. Results

All the datasets included in the study protocol were successfully analyzed using the presented pipeline.

3.1. Data reliability

Both reliability and cost-effectiveness of the dedicated processing were tested on a subgroup of randomly selected 15 patients, i.e., $^1/_3$ of the overall study population. For the manual processing of each dataset, the same LZ-specific cross-sections selected phase-by-phase within the 3D pipeline were manually segmented by an expert operator. The OF-based automated approach, as calculated in terms of area and perimeter (Fig. 2), reported excellent agreement ($r^2 = 0.99$ for both) against to manual processing with almost no bias, i.e., < 1%, and low variations (Bland-Altman limits of agreement between −8.6% and 9.5% for area and between −5.3% and 5.3% for perimeter). In terms of time efficiency, the automatic OF-based tracking and processing of a dataset consisting of 3 LZ planes took less than 90 s using a single Intel® Core i7–7700 (3.60 GHz, RAM 32 GB) processing unit. Consequently, the entire automated 3D pipeline required less than 8 min to complete the processing, from data input to geometrical output, for a patient-specific dataset. In contrast, manual annotation of the same number of images alone takes approximately 30 min.

3.2. Static vs. OF-based dynamic analysis

On a subgroup of 15 patients, randomly selected from the overall study population, the effect of OF-based adaptive analysis of LZ planes was quantified in terms of both area and perimeter (Fig. 2c) with respect to the corresponding measurements extracted from the static analysis of initially defined (phase 0) LZ planes only, i.e., fixing both position and orientation of each LZ plane over the cardiac cycle. The static analysis underestimated OF-based measurements with a bias below 2%; Bland-Altman limits of agreement were between −21.6% and 17.7% for area and between −12.2% and 9.5% for perimeter; the largest differences correspond to a variation in D_A and D_P no larger than 7 mm.

3.3. Geometrical LZ analysis

The quantitative analysis of LZ geometrical parameters revealed significant differences between TPVI and SPVR groups ($P < 0.0001$) for all the collected parameters, except for e, with larger LZ dimensions for SPVR group with respect to TPVI group (Fig. 3); significant differences also arose when comparing the different LZ planes. Specifically, equivalent diameters D_A and D_P were largely above 30 mm in SPVR group: D_A average value increase with respect to the corresponding value in TPVI group ranged between 15.7% (A_{MAX} on $\pi_{SA,D}$) and 31.3% (A_{min} on $\pi_{SA,M}$); similarly, D_P average value increase in SPVR group ranged between 14.9% (P_{MAX} on $\pi_{SA,D}$) and 30.7% (P_{min} on $\pi_{SA,M}$).

When comparing the different LZ locations, LZ dimensions proved to progressively reduce in SPVR moving from the proximal to the distal LZ position; conversely, in TPVI group, the smallest LZ dimension was generally revealed by the mid LZ location. This difference proved to be consistent with the RVOT morphological classification of patients in both the groups, with TPVI group reporting a higher presence of patients with Type V, i.e., narrowed centrally, RVOT anatomy (34.8% in TPVI vs. 13.6% in SPVR, Table 1).

D_H values, as averaged within each group, ranged from 27.8 mm ($D_{H,min}$ on $\pi_{SA,D}$) to 35.3 mm ($D_{H,MAX}$ on $\pi_{SA,P}$) in SPVR group and from 22.1 mm ($D_{H,min}$ on $\pi_{SA,M}$) to 29.7 mm ($D_{H,MAX}$ on $\pi_{SA,P}$) in TPVI group; D_H average increase in SPVR was consistent with the corresponding percentage D_A and D_P variations (Table S2). Larger LZ dimensions in SPVR group also reflected in higher values for both *MA* and *ma* semi-axes with

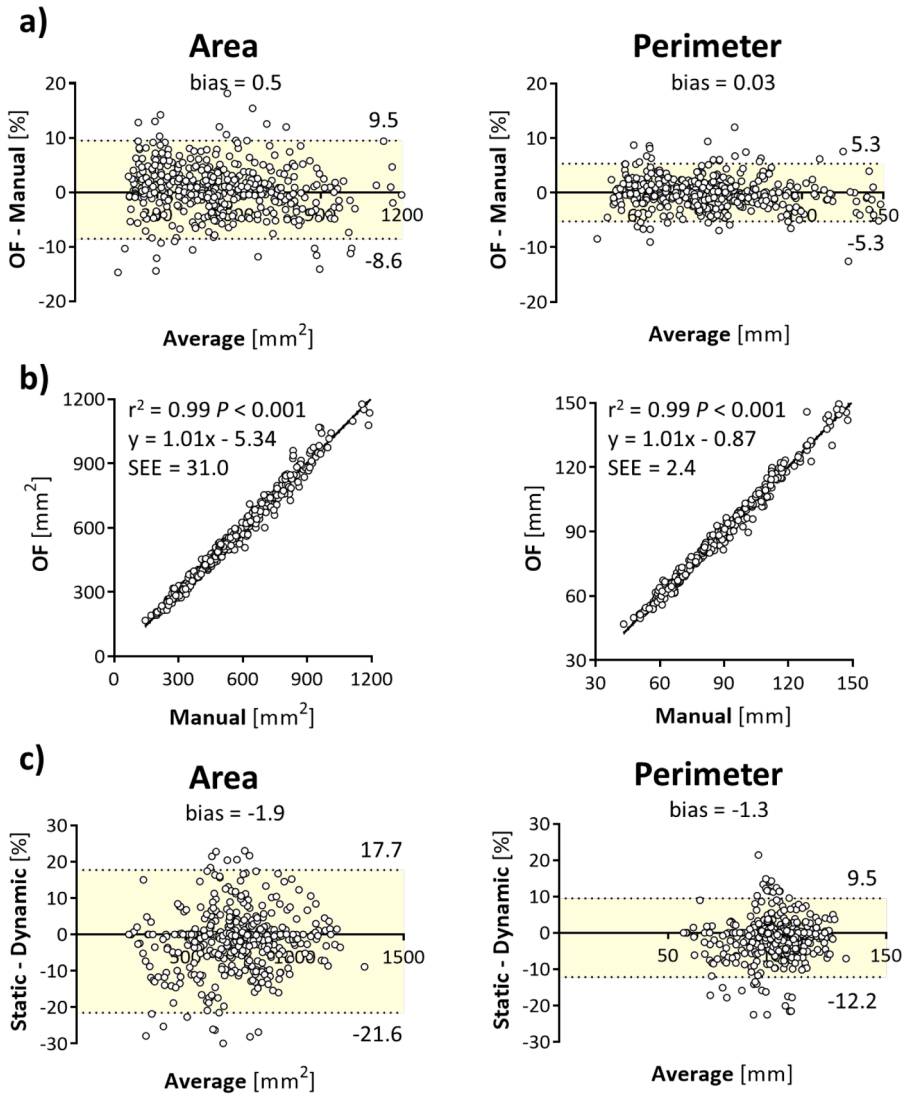

Fig. 2. Bland-Altman plots (a) and linear relation (b) between OF-based tracking and manual segmentation in terms of area and perimeter; (c) Bland-Altman plots of the difference in LZ measurements when comparing the analysis of a static cross-section with the one from dynamic analysis based on optical flow.

respect to TPVI group while *e* remained comparable ($P \geq 0.17$) between the two groups (Table S3). No significant differences were noticed, for each LZ parameter, in terms of percentage relative change over the cardiac cycle ($P \geq 0.17$, Table S4).

3.4. Likelihood of TPVI feasibility

Morphological covariates affecting the odds of TPVI feasibility, as identified by means of standard logistic regression, are highlighted in Fig. 4. All the analyzed LZ parameters reported a statistically significant effect on the likelihood of TPVI on $\pi_{SA,M}$ only; all the odds ratios computed on $\pi_{SA,M}$ were less than one, thus underlining that an increase in the variable would decrease the likelihood of TPVI.

Notably, P_{min}, P_{mean}, MA_{min} and A_{min} reported a Nagelkerke R^2 (R_N^2) above 0.8 when assessing the power of explanation of each model. At ROC analysis, the same parameters reported the highest AUC values, with P_{min} reaching the highest value of 0.99, with accuracy and precision of 0.93 and 0.92, respectively.

Comparing the rate of correct classifications (i.e., the matching rate between predicted and observed TPVI/SPVR classification) for each parameter (Fig. 5), P_{min} and $D_{H,min}$ exhibited the highest rate with 42/45 (93.3%) correct classifications (Table S11), followed by A_{min}, P_{mean} and MA_{min} with a rate of correct matching of 41/45 (91.1%). The descriptors of minimum LZ dimension outperformed the ones quantifying the maximum LZ dimension, with the latter reporting a rate of correct classification ranging between 36/45 (80%, MA_{MAX}) and 40/45 (88.9%, A_{MAX}) while P_{MAX} reported a rate of 37/45 (82.2%) correct classifications.

The analysis of bimodal probability density functions revealed that no LZ parameter provided a clear separation between the two groups, with all Ashman's *D* values below the threshold of $D = 2$. (Fig. 6); P_{min} reached the highest Asman's *D* equal to 1.96.

4. Discussion

The complex and dynamic geometry of the native and patched RVOT often precludes the use of currently available devices for TPVI [10,22,33]. To expand both feasibility and benefit of on-label TPVI options, technology is continuously evolving with new devices specifically designed for the native RVOT, e.g., the Medtronic Harmony™, the Alterra Adaptive Prestent™ and the Venus P-valve™ [34,35]. Nonetheless, the role of CT imaging is crucial to comprehensively assess the anatomic substrate of the native RVOT, which has important implications for TPVI planning and valve selection [22].

To collect the recommended native RVOT reporting elements (e.g.,

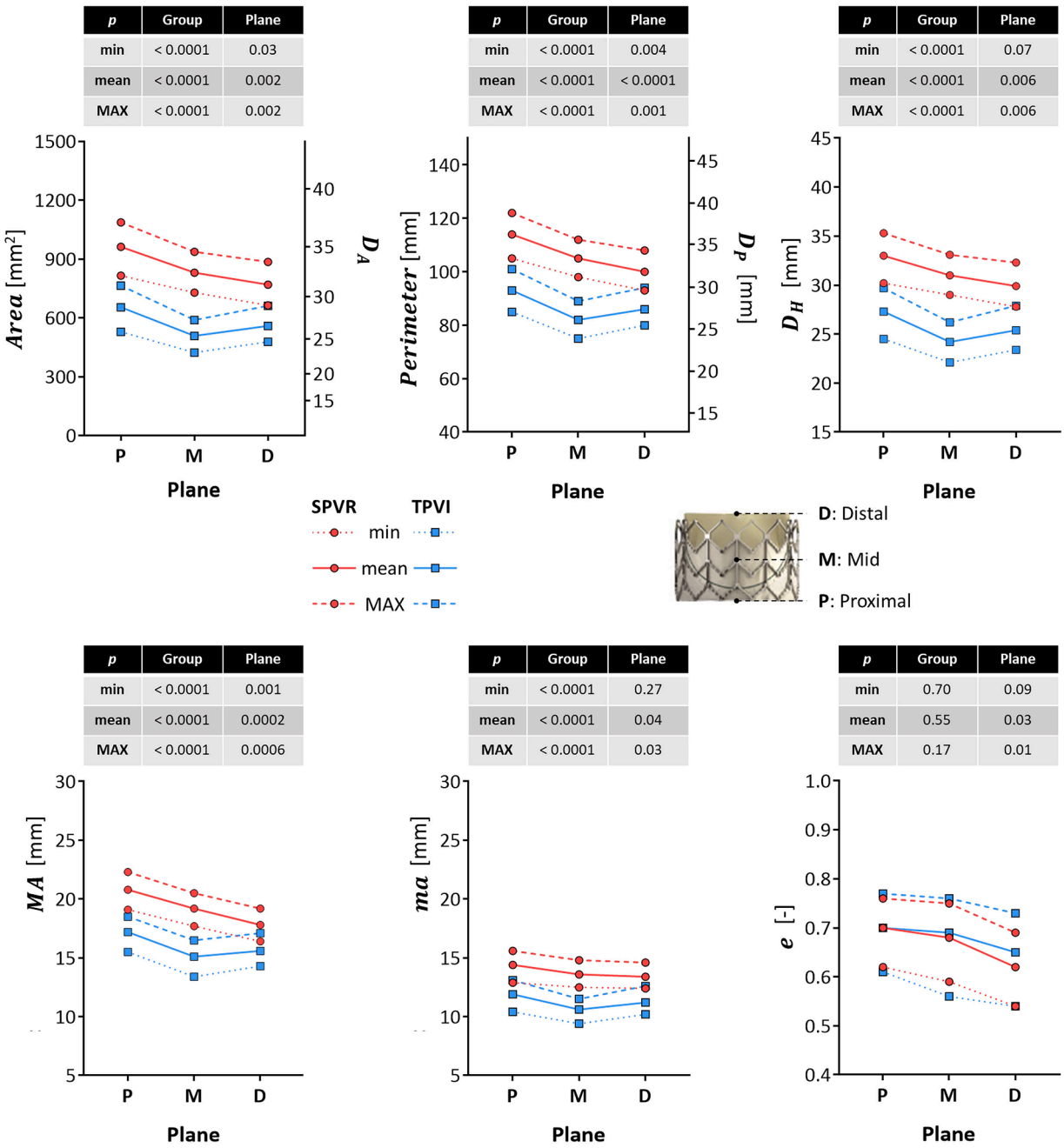

Fig. 3. Quantitative comparison of the main LZ geometrical parameters between SPVR and TPVI groups on each LZ plane, i.e., proximal (P), mid (M) and distal (D). For each plane, the average of minimum (dotted line), mean (continuous line) and maximum (dashed line) value distributions, as extracted over the cardiac cycle for each dataset, is reported for both TPVI and SPVR groups.

RVOT cross-sectional dimensions) for TPVI planning [22], a novel pipeline is herein proposed to facilitate and automatize preoperative analysis of the dysfunctional native RVOT anatomy.

4.1. Technical significance of the pipeline

The proposed pipeline proved to be effective in the dynamic assessment of RVOT cross-sectional changes, which can be automatically calculated over the cardiac cycle leveraging 4D CT imaging [19, 20]. Notably, the pipeline offers two main technical advantages.

First, the pipeline allows to take out-of-plane local movements, e.g., due to inherent cardiac motion, into account; all the cross-sections initially defined by the user are tracked over the cardiac cycle, adjusting both their position and orientation prior to elaborating RVOT geometric parameters.

Second, the dynamic RVOT analysis is automatized and does not require manual operations, thus avoiding the need for laborious, time-expensive and operator-dependent procedures to examine a single dataset [21].

If compared to ground truth manual segmentation, OF-based automatic segmentation of the RVOT inner vessel-wall proved to be adequate (Fig. 2a) as also confirmed by the statistically not significant differences between OF-based and manual tracing procedure for the calculation of both area ($P = 0.16$) and perimeter ($P = 0.52$) using the Wilcoxon signed-rank test reporting.

Availability of dynamic cross-sectional measurements allows to precisely identify and quantify the maximum RVOT dimension over the cardiac cycle; accordingly, the operator is no longer requested to

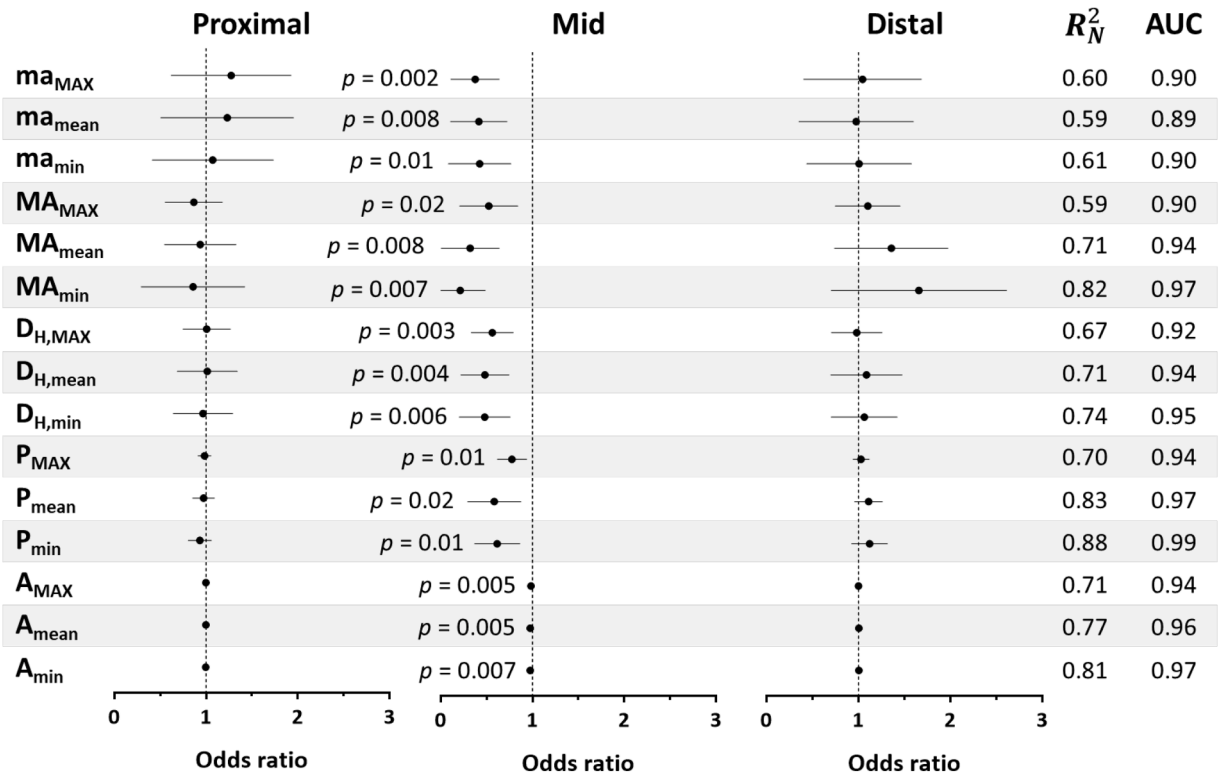

Fig. 4. Standard logistic regression for the identification of LZ morphological covariates affecting the odds of TPVI feasibility.

arbitrarily select a specific cardiac phase where RVOT cross-sectional area and perimeter are expected to be maximal [22]. The automatic analysis also evaluates the minimum RVOT dimension on the analyzed cross-section, thus providing additional insight into the range of RVOT dimensional variation over the cardiac cycle.

Hence, taking advantage of these technical features, the pipeline offers the possibility to guide 3D valve sizing within the LZ. Though beyond the purpose of the current analysis, the user can easily extend the LZ to analyze or increase the number of RVOT cross-sections. To meet clinical needs during procedure planning, a graphical representation of the perimeter-derived radius/diameter – namely referred to as the perimeter plot – has been recently proposed to assess device fit at any location between the subvalvar RVOT to the PA bifurcation [22,36–38]. As herein analyzed using three representative LZ cross-sections, the presented pipeline automatically generates these data and can also quantify the dynamic variation of the variable in terms of its minimum and maximum value over the cardiac cycle (Fig. 3). Also, the present pipeline can be adapted to guide selection and sizing of self-expandable valves, e.g., Alterra adaptive Prestent system (Edwards Lifesciences, Irvine, CA, USA), Harmony™ (Medtronic, Minneapolis, MN, USA), Pulsta® (TaeWoong Medical Co, Gyeonggido, South Korea) and Venus P-valve™ (Venus Medtech, Hangzhou, PRC) [10,39]. These devices are generally characterized by a stent significantly longer than the one of ballon-expandable valve with stent diameter progressively enlarging towards both the proximal and distal portions. Therefore, a comprehensive 3D assessment of patient-specific RVOT and PA anatomy is essential to identify the optimal match with a specific valve design, especially in the rapidly expanding market of THVs. This can significantly contribute to the identification of an adequate LZ and reduce the risk of valve malposition or embolization, which are well-known TPVI complications in patients with large RVOTs [11,40].

4.2. Clinical relevance and implications

As reported in a seminal study by Schievano and co-workers, the native RVOT is generally not circular but elliptical in cross-section [21] and, as also confirmed by the present analysis (Fig. 3), the oval RVOT cross-section can differ in both shape and size along the LZ with dynamic variations during the cardiac cycle.

Furthermore, during TPVI, THV deployment generally circularizes the shape of the native RVOT anatomy due to remarkable compliance exhibited by LZ wall tissues. Accordingly, simple measurements of the minimum or maximum diameters (e.g., the diameters along the minor and major axis of an ideal and oval RVOT cross-section, respectively) would inevitably lead to erroneous estimation of the true LZ size [41]. This further strengthens the importance of balloon interrogation of RVOT for precise valve size [42]. To address this knowledge gap, standardized diameters derived from perimeter and area calculations have been proposed as more reliable and reproducible metrics for guiding valve sizing [25,41,43]. According to our data, in both the SPVR and TPVI groups (Fig. 3), the values of *MA* and *ma* do not quantitatively represent the average diameter of the LZ cross-section, which can instead be better estimated in terms of D_P and D_A.

Ligon et al. also demonstrated a positive Spearman correlation ($r = 0.93$, $P < 0.01$) between D_P, referred to as "circularised" diameter, and the narrowest diameter of LZ region during balloon-testing [43]. Investigating appropriate device size selection in transcatheter aortic valve replacement, Halim and colleagues hypothesized that perimeter (as well as D_P) can be superior to area (and D_A) since less influenced by shape changes [44]. The data collected in the present analysis confirmed that similarity between D_P and D_A values varies depending on the shape of LZ cross-section (Fig. 7a): paired comparison showed that D_P values were significantly higher than D_A ones ($P < 0.0001$), with Bland-Altman analysis reporting a bias of 3.9% and limits of agreement ranging from −0.9% to +8.7%. Both TPVI and SPVR groups reported a comparable behavior; as illustrated in Fig. 7b, similarity between D_P and D_A values deteriorates as the LZ cross-section (i.e., the shape of the ellipse) becomes more elliptical, particularly when the eccentricity exceeds 0.7.

Therefore, in line with previous clinical evidence [25,43], these metrics warrant further investigation to assess their potential in

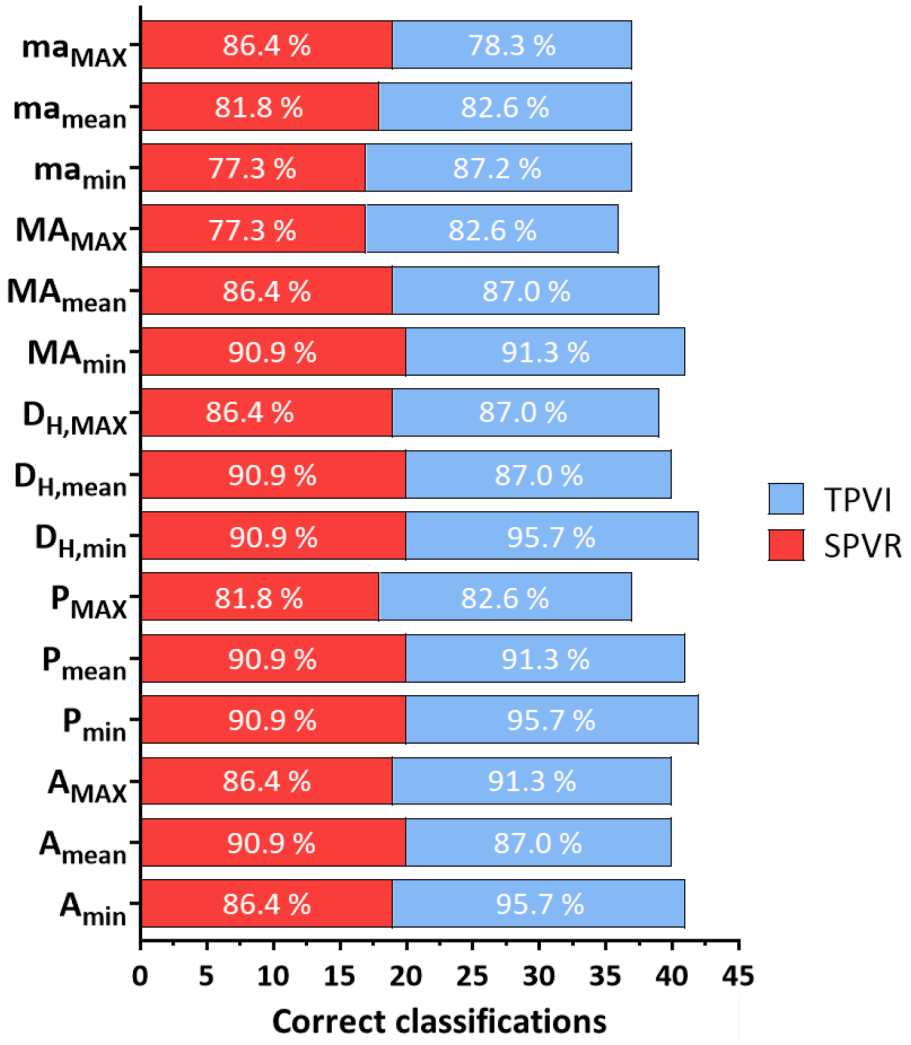

Fig. 5. Rate of correct classifications within each group, as achieved by each regression model with respect to the observed clinical classification.

predicting patient-specific suitability for a transcatheter procedure versus the necessity of a surgical intervention. To this end, using a retrospective cohort of TPVI recipients, the collected parameters were compared between the TPVI and SPVR groups, and the association of each parameter with the likelihood of TPVI feasibility was evaluated. From a clinical perspective, three key findings emerged from the analysis.

4.2.1. Relevance of LZ mid-plane ($\pi_{SA,M}$)

The LZ morphological covariates that significantly impact the likelihood of TPVI feasibility are primarily located at the mid-plane of the LZ ($\boldsymbol{\pi_{SA,M}}$), as shown by the results of standard logistic regression analysis (Fig. 4). It is worth noting that only patients implanted with a balloon-expandable THV, whose length is nominally shorter than self-expandable THVs, were considered in the current analysis. As a result, this finding cannot be generalized to all THVs used for TPVI and warrants further investigation, particularly concerning the self-expandable THVs that are increasingly becoming available on the market. Nonetheless, the comprehensive analysis of LZ morphology provided by the present pipeline can be useful during TPVI planning regardless of the specific type of THV that is going to be implanted. In the case of balloon-expandable THVs, the analysis also helps identify the LZ cross-section that reflects the true narrowest RVOT diameter. Although the compliance of the native or patched RVOT remains unpredictable, this cross-section is expected to represent the optimal target point for THV deployment, where the implant stability should be maximized. It should align with the precise location of the confirmatory waist, observed during balloon-sizing interrogation in the preliminary steps of the TPVI procedure [17].

4.2.2. Relevance of P_{min}

Among the available parameters, LZ perimeter (and the corresponding diameter D_P) proved to be the most effective in stratifying patients in terms of TPVI/SPVR candidacy, further corroborating the preliminary findings of Ligon et al. [43]. Furthermore, the analysis revealed that P_{min} outperformed all the other parameters, including P_{MAX}, in its ability to distinguish between TPVI and SPVR candidates: P_{min} reached the highest rate of correct classifications (i.e., 95.7% for TPVI and 90.9% for SPVR, Fig. 5) and the highest Ashman's D of 1.96. If we design as "positive" the patients classified by our method as eligible to TPVI and as "negative" those classified as ineligible, based on P_{min} the model identified 22 true positives (TP), i.e., patients successfully treated with TPVI and correctly classified as eligible, and 16 true negatives (TN), i.e., patients sent to SPVR after peri-procedural catheterization and correctly classified as ineligible (Fig. 8). However, as evident from the corresponding bimodal probability density function (Fig. 6), there is significant overlap between the TPVI and SPVR distributions, which limits P_{min} ability to achieve a clear separation between the two groups (a marked separation is typically indicated by Ashman's D values greater than 2). Indeed, three misclassifications were observed (Fig. 8). One case

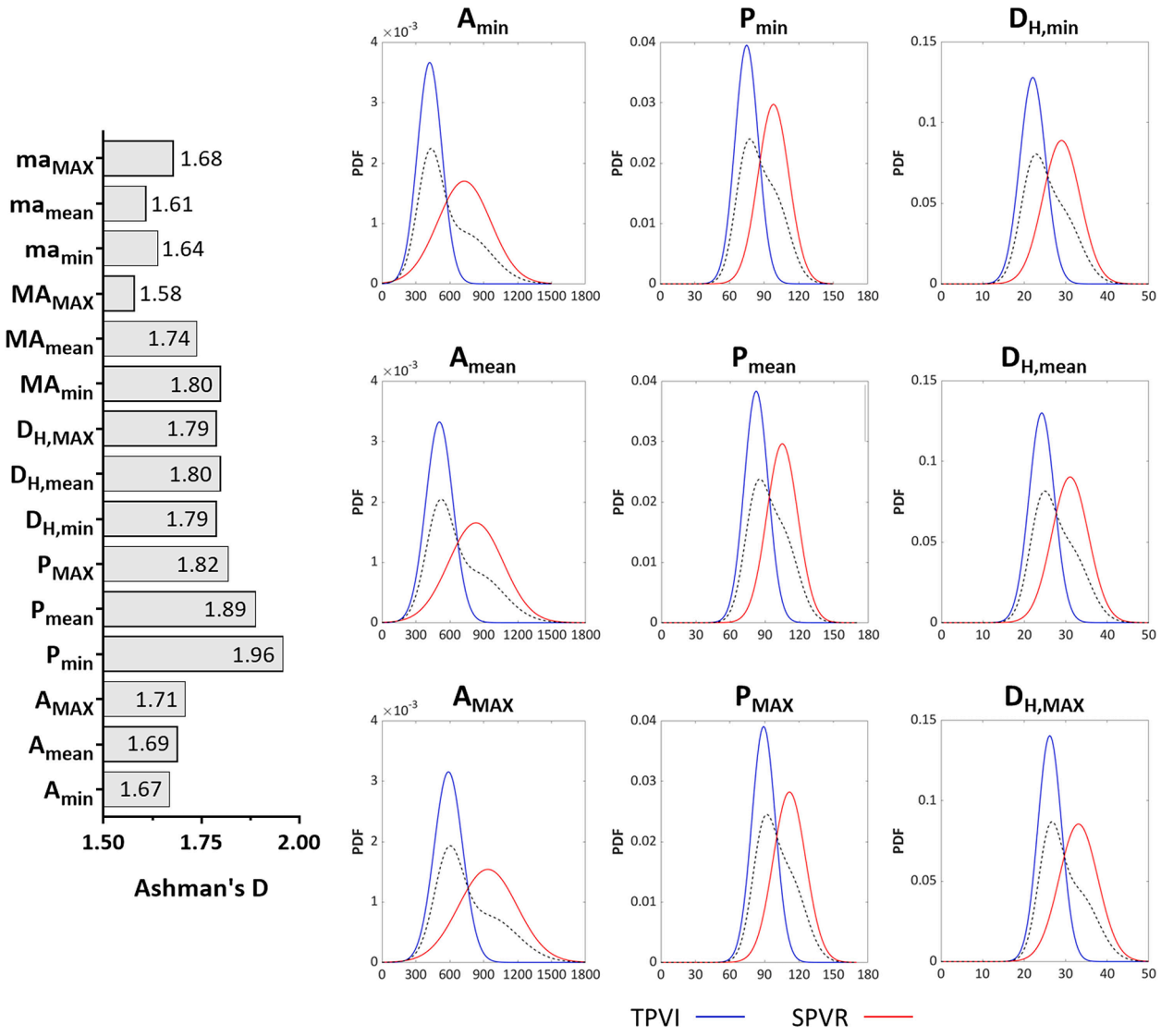

Fig. 6. Bimodal probability density functions computed for each descriptor of LZ geometry and the corresponding values of the Ashman's *D*.

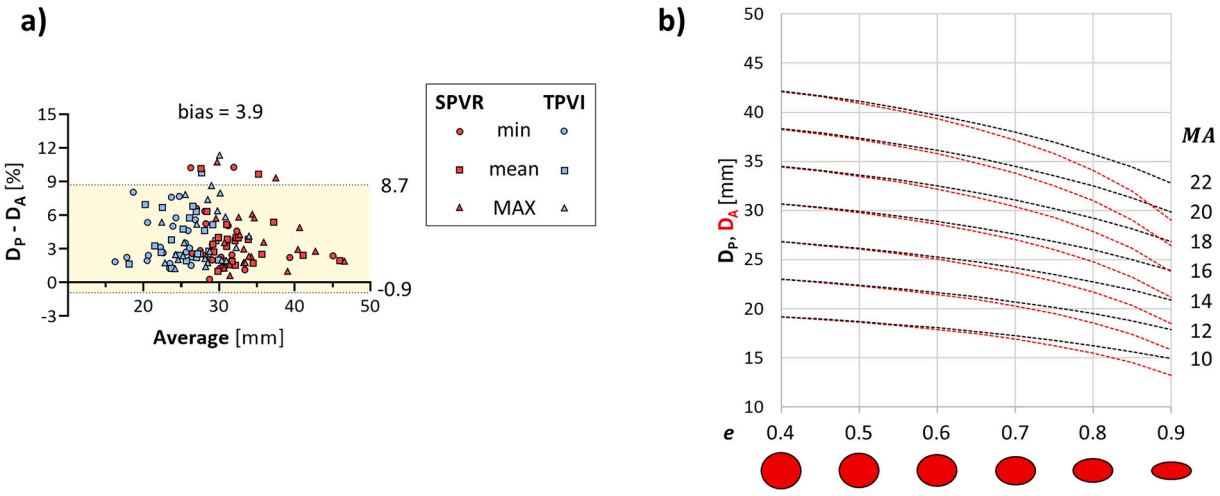

Fig. 7. Bland-Altman plot (a) of the percentage differences from measurements of LZ diameter based on perimeter (D_P) or area (D_A) on the LZ mid-plane ($\pi_{SA,M}$) of each dataset, including minimum, mean and maximum diameters; b) theoretical difference between D_P and D_A for an ellipse with a semi-major axis (MA) increasing from 10 to 22 mm and eccentricity (e) in the range 0.4 ÷ 0.9. Perimeter of ellipse estimated with Ramanujan approximation, $P \approx \pi\left[3(MA + ma) - \sqrt{(3 \cdot MA + ma)(MA + 3 \cdot ma)}\right]$.

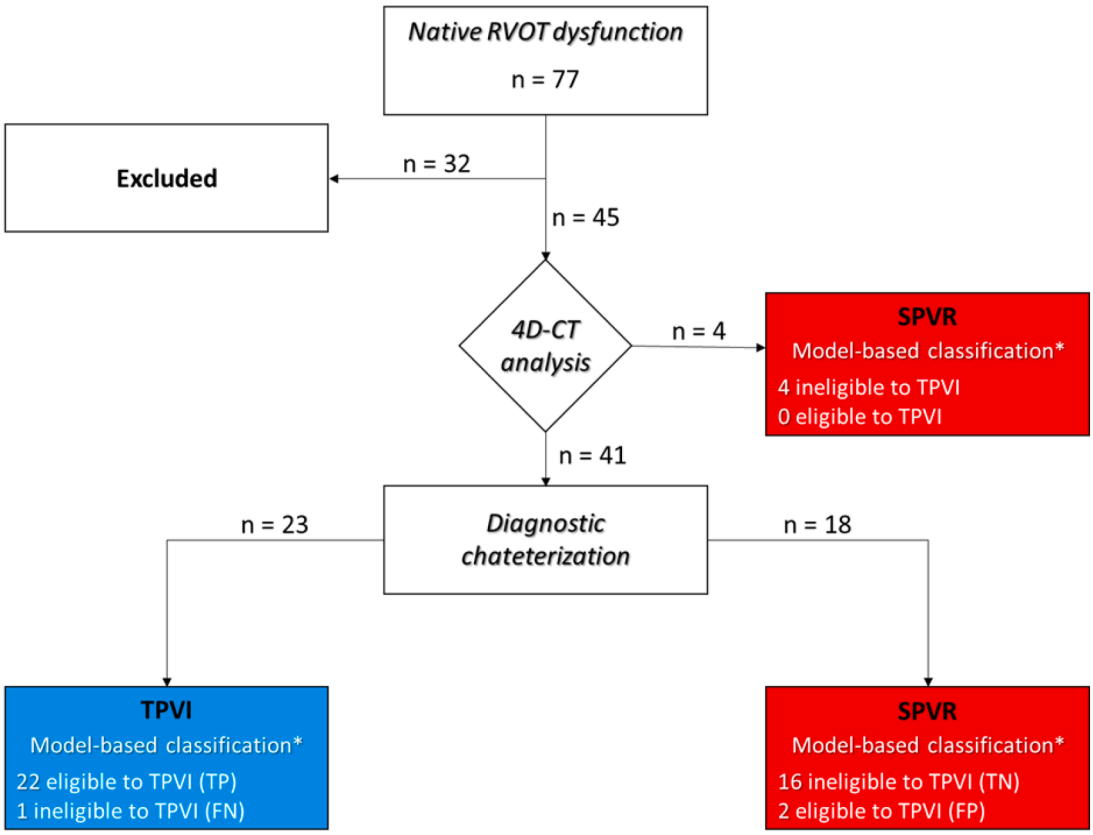

Fig. 8. Flowchart illustrating the clinical-based classification of the study population and the logistic model prediction outcomes from P_{min} (as well as the corresponding $D_{P,min}$) analysis (*) using automated LZ measurements. Patients who successfully underwent TPVI were classified as either eligible (true positives, TP) or ineligible (false negatives, FN) for TPVI. Conversely, patients who proceeded to SPVT following diagnostic catheterization were classified as eligible (false positives, FP) or ineligible (true negatives, TN) for TPVI.

was a false negative (FN), i.e., a patient successfully treated with TPVI but classified as ineligible by our automated analysis; this subject was characterized by a $D_{P,min}$ value of 29.6 mm on the LZ mid-section, which is borderline for balloon-expandable TPVI. This misclassification may reflect the overly cautious nature of our preliminary model predictions. The other two cases were false positives (FP), i.e., patients classified as eligible by our method but ultimately sent to SPVR after diagnostic catheterization. Although their $D_{P,min}$ values in the LZ mid-section - equal to 27.6 mm and 26.8 mm, respectively – can be considered suitable for TPVI, clinical evidence from diagnostic catheterization, e.g., lack of balloon indentation, revealed that the sizing balloon test results were deemed unsatisfactory by clinicians. Notably, patients selected for SPVR during the pre-procedural planning phase based on CT-based measurements could not be categorized as TN/FN or TP/FP. Despite these three misclassifications, P_{min} demonstrated a stronger protective effect compared to P_{MAX}, as reflected by the calculated ORs of 0.58 (0.39 ÷ 0.88) for P_{min} and 0.77 (0.62 ÷ 0.94) for P_{MAX}, respectively (Table S6). We can hence speculate that, for two RVOT anatomies with comparable P_{MAX} values, the LZ with a smaller P_{min} is likely to produce more favorable THV radial force and result in greater implant stability following TPVI with the same device. To this end, P_{min} might be recommended for planning TPVI in large native RVOTs, which are currently investigated mainly focusing on the maximum dimension in the cardiac cycle along the length of the potential LZ [22]. To this end, it is worth stressing that the pipeline's ability to automate P_{min} extraction across the entire cardiac cycle ensures that this parameter can be readily available to clinicians within a timeframe suitable for procedural planning.

4.2.3. Relevance of dynamic LZ analysis

By comparing the results of static and dynamic sensitivity analysis, paired comparison revealed statistically significant differences both in terms of P ($P < 0.0001$) and A ($P < 0.0001$); the maximum axial displacement along the vessel centerline of the dynamic planes varies between 3 and 22 mm, closely matching the range of 2 to 18 mm reported by Schievano et al. using a manual procedure [21]. From a clinical perspective, the mean difference between static and dynamic measurements results in an underestimation of approximately 0.3 mm for both D_P and D_A when using static planes, with a potentially negligible clinical impact. However, the limits of agreement for these differences are remarkable ($-2.7 \div 2.0$ mm for D_P and $-2.1 \div 1.5$ mm for D_A), warranting further and more extensive clinical validation. Indeed, an underestimation of the true LZ dimension could expose the patient, e.g., a patient with large though apparently suitable RVOT anatomy (false positive classification), to the risk of an unsuccessful TPVI with high risk of implant embolization or instability. Conversely, overestimating the LZ dimension may prevent the patient, e.g., a patient with large and borderline RVOT anatomy (false negative classification), from benefiting from the TPVI procedure.

4.3. Limitations and future work

The major limitation of this study is related to its retrospective nature and relatively small sample size. The preliminary evidence we obtained in our monocentric analysis strongly suggests the effectiveness of the proposed pipeline in the assessment of native RVOT anatomy. However, given the limited annual rate of patients with dysfunctional native RVOT requiring TPVI, a multicenter, prospective clinical trial would be crucial to expand the analysis, ensure a sound evaluation of our model and

improve its accuracy in classifying suitable candidates for TPVI.

Also, from a clinical perspective, this study lacks a gold-standard pre-procedural planning method for patient classification, primarily due to its retrospective design. Although measurements were taken from pre-procedural CT scans, they were not performed following a standardized protocol. As a result, the classifications generated by our method were compared against the final clinical decision, which served as the reference standard. Importantly, technical guidelines for CT-based TPVI planning, such as those outlined by Han et al. [22], now provide a more structured framework for clinical decision-making by recommending a detailed set of reporting elements for native RVOT evaluation. While the TPVI decision-making process cannot be entirely replaced by a deterministic model, adopting automated, systematic and standardized approaches for pre-TPVI assessment of native RVOT anatomy can significantly improve candidate selection and offer deeper insights into the factors affecting TPVI feasibility.

From a technical standpoint, the following limitations should be considered when interpreting the results of the study.

First, the user is currently required to manually initialize the analysis by providing the CT-derived RVOT surface and its centerline. To address this limitation, efforts are underway to automate the process using a deep learning-based segmentation model, such as TotalSegmentator (www.totalsegmentator.com) that has already shown robust results in reproducing cardiovascular structures from CT imaging [45].

Second, the dynamic analysis of LZ cross-sections throughout the cardiac cycle employs a 2D optical flow algorithm, providing a good balance between accuracy and computational efficiency. While 3D optical flow algorithms for capturing 3D heart deformation using dynamic CT have garnered interest in medical imaging analysis, challenges and potential of these 3D algorithms are yet to be fully analyzed [46] and the total computation time is still relatively long [47].

Third, the position of each LZ transversal plane was dynamically adjusted throughout the cardiac cycle by applying the same axial displacement, as calculated on $\boldsymbol{\Gamma}_{LA,1}$ and $\boldsymbol{\Gamma}_{LA,2}$ at each cardiac phase along the entire RVOT/PA anatomy, thereby neglecting more localized effects due to RVOT wall motion. This assumption guarantees a consistent analysis along a predefined LZ extension matching the specific THV length; nonetheless, further extensive analysis on a larger population is needed to better understand the impact of RVOT anatomical complexity and shape variability, e.g., by including patients with type IV RVOT morphology [23].

Fourth, although it can spare clinicians from complex, time-consuming, and operator-dependent procedures, the presented pipeline is not yet implemented as an easy-to-use digital platform, which would be essential for its use by radiologists or interventional cardiologists in different centers. To perform this extra step, the codes we implemented in Matlab should become a standalone tool based on open source compiled language (e.g., Python) that does not require access to commercial scientific software, and software engineering and extensive testing would be required.

Fifth, the proposed pipeline provides cross-sectional area and perimeter data throughout the cardiac cycle, but biomechanical indices like compliance cannot be calculated due to the lack of the patient-specific pressure waveform. Even if pressure waveforms were available during 4D-CT, estimating compliance and relating it to the outcomes of the sizing procedure remains difficult given that the RVOT/PA experiences low pressures during 4D-CT compared to the higher pressures during the sizing procedure. Since the stress-strain response of vessel wall tissue is expected to remain non-linear in the dysfunctional native RVOT, despite its frequent non-physiological remodeling due to the presence of a patch, the estimated compliance would not be representative of the vessel compliance during the sizing procedure. In this context, ongoing efforts focus on further elaborating 3D displacements of the vertices in the triangulated RVOT/PA surface to yield the strain field on the vessel wall, potentially revealing heterogeneities in wall distensibility and identifying particularly compliant regions of the vessel wall, which could influence implant stability.

5. Conclusions

We presented a time efficient pipeline for analyzing the dysfunctional native RVOT anatomy throughout the cardiac cycle, leveraging 4D-CT imaging. The pipeline can enhance the accuracy of RVOT anatomical evaluation and improve TPVI planning procedure by aiding in the more effective selection of TPVI candidates and reducing the use of radiation and contrast-agents during the catheterization. By leveraging the novel photon-counting CT technology [48,49], which enhances image quality while reducing dose radiation, the potential of the present pipeline could be further consolidated and also extended to the quantification and monitoring of native RVOT growth [50].

Ethics statement

The study was approved by the local Ethics Committee (research protocol code “4D_Native_RVOT”, No. 56/INT/2022, accepted on June 24th 2022). Informed consent was waived due to the retrospective nature of the study and the analysis of anonymized data. The study was conducted in compliance with the Good Clinical Practice and Declaration of Helsinki principles.

Data availability

The data that support the findings of this study are available from the corresponding author upon reasonable request.

CRediT authorship contribution statement

Francesco Sturla: Writing – original draft, Project administration, Methodology, Formal analysis, Conceptualization. **Alessandro Caimi:** Writing – original draft, Validation, Methodology, Conceptualization. **Luca Giugno:** Writing – review & editing, Methodology, Data curation. **Giulia Pasqualin:** Writing – review & editing, Visualization, Data curation. **Karima Tissir:** Resources, Formal analysis, Data curation. **Francesco Secchi:** Visualization, Resources, Data curation. **Alberto Redaelli:** Writing – review & editing, Resources, Investigation, Funding acquisition. **Mario Carminati:** Writing – review & editing, Supervision, Investigation, Funding acquisition. **Emiliano Votta:** Writing – review & editing, Supervision, Methodology, Conceptualization.

Declaration of competing interest

The authors declare that they have no known competing financial interests or personal relationships that could have appeared to influence the work reported in this paper.

Acknowledgements

The financial support of “Ricerca Corrente” grant from IRCCS Policlinico San Donato, which is a clinical research hospital partially funded by the Italian Ministry of Health, is gratefully acknowledged.

Supplementary materials

Supplementary material associated with this article can be found, in the online version, at doi:10.1016/j.cmpb.2024.108569.

References

[1] S. Hascoët, P. Acar, Y. Boudjemline, Transcatheter pulmonary valvulation: current indications and available devices, Arch. Cardiovasc. Dis. 107 (11) (2014) 625–634, https://doi.org/10.1016/j.acvd.2014.07.048.

[2] J. Therrien, G. Webb, Clinical update on adults with congenital heart disease, Lancet 362 (9392) (2003) 1305–1313, https://doi.org/10.1016/s0140-6736(03)14574-6.

[3] G. Nollert, T. Fischlein, S. Bouterwek, et al., Long-term survival in patients with repair of tetralogy of Fallot: 36-year follow-up of 490 survivors of the first year after surgical repair, J. Am. Coll. Cardiol. 30 (5) (1997) 1374–1383, https://doi.org/10.1016/s0735-1097(97)00318-5.

[4] J.L.R. Romeo, J.R.G. Etnel, J.J.M. Takkenberg, et al., Outcome after surgical repair of tetralogy of Fallot: a systematic review and meta-analysis, J. Thorac. Cardiovasc. Surg. 159 (1) (2020) 220–236, https://doi.org/10.1016/j.jtcvs.2019.08.127. . e228.

[5] H.G. Freling, T.P. Willems, J.P. van Melle, et al., Effect of right ventricular outflow tract obstruction on right ventricular volumes and exercise capacity in patients with repaired tetralogy of fallot, Am. J. Cardiol. 113 (4) (2014) 719–723, https://doi.org/10.1016/j.amjcard.2013.10.049.

[6] M.M. Ansari, R. Cardoso, D. Garcia, et al., Percutaneous Pulmonary Valve Implantation: present Status and Evolving Future, J. Am. Coll. Cardiol. 66 (20) (2015) 2246–2255, https://doi.org/10.1016/j.jacc.2015.09.055.

[7] L. Malone, B. Fonseca, T. Fagan, et al., Preprocedural Risk Assessment Prior to PPVI with CMR and Cardiac CT, Pediatr. Cardiol. 38 (4) (2017) 746–753, https://doi.org/10.1007/s00246-017-1574-0.

[8] N.A. Haas, R. Vcasna, K.T. Laser, et al., The standing of percutaneous pulmonary valve implantation compared to surgery in a non-preselected cohort with dysfunctional right ventricular outflow tract – Reasons for failure and contraindications, J. Cardiol. 74 (3) (2019) 217–222, https://doi.org/10.1016/j.jjcc.2019.03.021.

[9] P. Bonhoeffer, Y. Boudjemline, Z. Saliba, et al., Percutaneous replacement of pulmonary valve in a right-ventricle to pulmonary-artery prosthetic conduit with valve dysfunction, Lancet 356 (9239) (2000) 1403–1405, https://doi.org/10.1016/s0140-6736(00)02844-0.

[10] N.D. Patel, D.S. Levi, J.P. Cheatham, et al., Transcatheter pulmonary valve replacement: a review of current valve technologies, J. Soc. Cardiovasc. Angiogr. Interv. 1 (6) (2022) 100452, https://doi.org/10.1016/j.jscai.2022.100452.

[11] M.H. Martin, J. Meadows, D.B. McElhinney, et al., Safety and feasibility of melody transcatheter pulmonary valve replacement in the native right ventricular outflow tract: a multicenter pediatric heart network scholar study, JACC Cardiov. Int. 11 (16) (2018) 1642–1650, https://doi.org/10.1016/j.jcin.2018.05.051.

[12] A. Houeijeh, C. Batteux, C. Karsenty, et al., Long-term outcomes of transcatheter pulmonary valve implantation with melody and SAPIEN valves, Int. J. Cardiol. 370 (2023) 156–166, https://doi.org/10.1016/j.ijcard.2022.10.141.

[13] S. Hascoet, R.D. Pozza, J. Bentham, et al., Early outcomes of percutaneous pulmonary valve implantation using the Edwards SAPIEN 3 transcatheter heart valve system, EuroIntervention. 14 (13) (2019) 1378–1385, https://doi.org/10.4244/EIJ-D-18-01035.

[14] A. Fraisse, A. Kempny, C. Bautista-Rodriguez, Outcome after transcatheter pulmonary valve replacement: are we focusing on the long term now? J. Am. Coll. Cardiol. 79 (1) (2022) 33–34, https://doi.org/10.1016/j.jacc.2021.10.032.

[15] E. Odemis, I. Yenidogan, First experiences with Myval Transcatheter Heart Valve System in the treatment of severe pulmonary regurgitation in native right ventricular outflow tract and conduit dysfunction, Cardiol. Young. 32 (10) (2022) 1609–1615, https://doi.org/10.1017/s1047951121004650.

[16] Y. Boudjemline, G. Sarquella-Brugada, I. Kamache, et al., Impact of right ventricular outflow tract size and substrate on outcomes of percutaneous pulmonary valve implantation, Arch. Cardiovasc. Dis. 106 (1) (2013) 19–26, https://doi.org/10.1016/j.acvd.2012.09.005.

[17] M. Álvarez-Fuente, M. Toledano, E. Garrido-Lestache, et al., Balloon-expandable pulmonary valves for patched or native right ventricular outflow tracts, Pediatr. Cardiol. 44 (6) (2023) 1285–1292, https://doi.org/10.1007/s00246-023-03173-2.

[18] M. Chessa, G. Butera, L. Giugno, et al., Percutaneous pulmonary valve implantation in a single artery branch: a preliminary experience, World J. Cardiol. 7 (10) (2015) 695–699, https://doi.org/10.4330/wjc.v7.i10.695.

[19] A. Canan, D. Ocazionez-Trujillo, D. Vargas, et al., Pre- and postprocedure imaging of transcatheter pulmonary valve implantation, Radiographics. 42 (4) (2022) 991–1011, https://doi.org/10.1148/rg.210160.

[20] R. Chung, A.M. Taylor, Imaging for preintervention planning transcatheter pulmonary valve therapy, Circul. Cardiov. Imaging 7 (1) (2014) 182–189, https://doi.org/10.1161/CIRCIMAGING.113.000826.

[21] S. Schievano, C. Capelli, C. Young, et al., Four-dimensional computed tomography: a method of assessing right ventricular outflow tract and pulmonary artery deformations throughout the cardiac cycle, Eur. Radiol. 21 (1) (2011) 36–45, https://doi.org/10.1007/s00330-010-1913-5.

[22] B.K. Han, S. Garcia, J. Aboulhosn, et al., Technical recommendations for computed tomography guidance of intervention in the right ventricular outflow tract: native RVOT, conduits and bioprosthetic valves:: A white paper of the Society of Cardiovascular Computed Tomography (SCCT), Congenital Heart Surgeons' Society (CHSS), and Society for Cardiovascular Angiography & Interventions (SCAI), J. Cardiovasc. Comput. Tomogr. (2023), https://doi.org/10.1016/j.jcct.2023.06.005.

[23] S. Schievano, L. Coats, F. Migliavacca, et al., Variations in right ventricular outflow tract morphology following repair of congenital heart disease: implications for percutaneous pulmonary valve implantation, J. Cardiovasc. Magn. Reson. 9 (4) (2007) 687–695, https://doi.org/10.1080/10976640601187596.

[24] M.C. Sivaprakasam, J.R.V. Reddy, R. Ganesan, et al., Choosing an appropriate size valve for transcatheter pulmonary valve implantation in a native right ventricle outflow tract, Ann. Pediatr. Cardiol. 15 (2) (2022) 154–159, https://doi.org/10.4103/apc.apc_62_21.

[25] L. Curran, H. Agrawal, K. Kallianos, et al., Computed tomography guided sizing for transcatheter pulmonary valve replacement, IJC Heart Vascul. 29 (2020) 100523, https://doi.org/10.1016/j.ijcha.2020.100523.

[26] F.R. Pluchinotta, F. Sturla, A. Caimi, et al., 3-Dimensional personalized planning for transcatheter pulmonary valve implantation in a dysfunctional right ventricular outflow tract, Int. J. Cardiol. 309 (2020) 33–39, https://doi.org/10.1016/j.ijcard.2019.12.006.

[27] A. Savitzky, M.J.E. Golay, Smoothing and differentiation of data by simplified least squares procedures, Anal. Chem. 36 (8) (1964) 1627–1639, https://doi.org/10.1021/ac60214a047.

[28] C. Liu, Beyond Pixels, Exploring New Representations and Applications for Motion Analysis, Massachusetts Institute of Technology, Boston, MA, USA, 2009.

[29] J. Shum, G. Martufi, E. Di Martino, et al., Quantitative assessment of abdominal aortic aneurysm geometry, Ann. Biomed. Eng. 39 (1) (2011) 277–286, https://doi.org/10.1007/s10439-010-0175-3.

[30] A.W. Fitzgibbon, M. Pilu, R.B. Fisher, Direct least squares fitting of ellipses, in: Proceedings of 13th International Conference on Pattern Recognition 251, 1996, pp. 253–257.

[31] W.H. Kamr, A.M. El-Tantawy, M.M. Harraz, et al., Pulmonary embolism: low dose contrast MSCT pulmonary angiography with modified test bolus technique, Eur. J. Radiol. Open. 7 (2020) 100254, https://doi.org/10.1016/j.ejro.2020.100254.

[32] J. Bondesson, G.-Y. Suh, T. Lundh, et al., Quantification of true lumen helical morphology and chirality in type B aortic dissections, Am. J. Physiol. Heart Circulat. Physiol. 320 (2) (2021) H901–H911, https://doi.org/10.1152/ajpheart.00778.2020.

[33] A. Kheiwa, P. Divanji, V.S. Mahadevan, Transcatheter pulmonary valve implantation: will it replace surgical pulmonary valve replacement? Expert. Rev. Cardiovasc. Ther. 16 (3) (2018) 197–207, https://doi.org/10.1080/14779072.2018.1435273.

[34] S. Shahanavaz, J. Tang, M.J. Gillespie, et al., Emerging solutions for the dilated native right ventricular outflow tract, Prog. Pediatr. Cardiol. 61 (2021) 101369, https://doi.org/10.1016/j.ppedcard.2021.101369.

[35] P. Tannous, A. Nugent, Transcatheter pulmonary valve replacement in native and nonconduit right ventricle outflow tracts, J. Thorac. Cardiovasc. Surg. 162 (3) (2021) 967–970, https://doi.org/10.1016/j.jtcvs.2020.07.126.

[36] D.B. McElhinney, M.J. Gillespie, J.A. Aboulhosn, et al., Transcatheter pulmonary valve replacement with the harmony valve in patients who do not meet recommended oversizing criteria on the screening perimeter plot, Circulat. Cardiov. Int. 17 (5) (2024) e013889, https://doi.org/10.1161/CIRCINTERVENTIONS.123.013889.

[37] E. Mejia, K. O'Neill, J.S. Lozier, et al., Self-Expanding Transcatheter Pulmonary Valve Implant in the Right Pulmonary Artery, JACC: Case Rep. 14 (2023) 101823, https://doi.org/10.1016/j.jaccas.2023.101823.

[38] S. Shahanavaz, D. Balzer, V. Babaliaros, et al., Alterra Adaptive Prestent and SAPIEN 3 THV for congenital pulmonic valve dysfunction: an early feasibility study, JACC: Card Int 13 (21) (2020) 2510–2524, https://doi.org/10.1016/j.jcin.2020.06.039.

[39] N. Agwu, M.R. Recto, A. Kheradvar, Unmet clinical needs for transcatheter pulmonary valves, Ann. Biomed. Eng. (2023), https://doi.org/10.1007/s10439-023-03328-5.

[40] D. Zhou, W. Pan, H. Jilaihawi, et al., A self-expanding percutaneous valve for patients with pulmonary regurgitation and an enlarged native right ventricular outflow tract: one-year results, EuroIntervention 14 (13) (2019) 1371–1377, https://doi.org/10.4244/eij-D-18-00715.

[41] S. Ebel, S. Gottschling, M.T.A. Buzan, et al., 3D-assessment of RVOT dimensions prior percutaneous pulmonary valve implantation: comparison of contrast-enhanced magnetic resonance angiography versus 3D steady-state free precession sequence, Int. J. Cardiovasc. ImAging 35 (8) (2019) 1453–1463, https://doi.org/10.1007/s10554-019-01578-w.

[42] W.-C. Shen, C.-A. Chen, C.-I. Chang, et al., Outflow tract geometries are associated with adverse outcome indicators in repaired tetralogy of Fallot, J. Thorac. Cardiovasc. Surg. 162 (1) (2021) 196–205, https://doi.org/10.1016/j.jtcvs.2020.09.072.

[43] R.A. Ligon, L.A. Latson, M.M. Ruzmetov, et al., Right ventricular outflow tract landing zone perimeter /circularised diameter – new imaging standards in pulmonary valve replacement reporting, Cardiol. Young. 33 (10) (2022) 1840–1845, https://doi.org/10.1017/S1047951122003286.

[44] J. Halim, P. den Heijer, J. Vos, et al., Balloon-Expandable TAVR bioprostheses: area or perimeter sizing? a prospective pilot study, J. Interv. Cardiol. 2022 (2022) 3139476, https://doi.org/10.1155/2022/3139476.

[45] J. Wasserthal, H.-C. Breit, M.T. Meyer, et al., TotalSegmentator: robust segmentation of 104 anatomic structures in CT images, Radiol. Artif. Intell. 5 (5) (2023) e230024, https://doi.org/10.1148/ryai.230024.

[46] A. Bab-Hadiashar, R.B. Tennakoon, M. deBruijne, Quantification of smoothing requirement for 3D optic flow calculation of volumetric images, IEEE Trans. Image Process. 22 (6) (2013) 2128–2137, https://doi.org/10.1109/TIP.2013.2246174.

[47] D. Yang, W. Lu, D.A. Low, et al., 4D-CT motion estimation using deformable image registration and 5D respiratory motion modeling, Med. Phys. 35 (10) (2008) 4577–4590, https://doi.org/10.1118/1.2977828.

[48] T. Dirrichs, E. Tietz, A. Rüffer, et al., Photon-counting versus dual-source CT of congenital heart defects in neonates and infants: initial experience, Radiology 307 (5) (2023) e223088, https://doi.org/10.1148/radiol.223088.
[49] P.S. Rajiah, H. Alkadhi, N.M. Van Mieghem, et al., Utility of photon counting ct in transcatheter structural heart disease interventions, Semin. Roentgenol. 59 (1) (2024) 32–43, https://doi.org/10.1053/j.ro.2023.11.005.
[50] K. Jurow, K. Gauvreau, N. Maschietto, et al., Growth of the right ventricular outflow tract in repaired tetralogy of Fallot: a longitudinal CMR study, J. Cardiov. Magnet. Reson. 26 (1) (2024) 100002, https://doi.org/10.1016/j.jocmr.2023.100002.